Monthly Notices
of the
ROYAL ASTRONOMICAL SOCIETY

MNRAS **459,** 3783–3791 (2016)
Advance Access publication 2016 April 29

doi:10.1093/mnras/stw883

Simulated gamma-ray pulse profile of the Crab pulsar with the Cherenkov Telescope Array

A. Burtovoi[1,2]★ and L. Zampieri[2]★

[1]*Department of Physics and Astronomy, University of Padova, vicolo dell' Osservatorio 3, I-35122 Padova, Italy*
[2]*INAF – Astronomical Observatory of Padova, vicolo dell' Osservatorio 5, I-35122 Padova, Italy*

Accepted 2016 April 13. Received 2016 April 12; in original form 2015 November 3

ABSTRACT

We present simulations of the very high energy (VHE) gamma-ray light curve of the Crab pulsar as observed by the Cherenkov Telescope Array (CTA). The CTA pulse profile of the Crab pulsar is simulated with the specific goal of determining the accuracy of the position of the interpulse. We fit the pulse shape obtained by the Major Atmospheric Gamma-Ray Imaging Cherenkov (MAGIC) telescope with a three-Gaussian template and rescale it to account for the different CTA instrumental and observational configurations. Simulations are performed for different configurations of CTA and for the ASTRI (Astrofisica con Specchi a Tecnologia Replicante Italiana) mini-array. The northern CTA configuration will provide an improvement of a factor of ∼3 in accuracy with an observing time comparable to that of MAGIC (73 h). Unless the VHE spectrum above 1 TeV behaves differently from what we presently know, unreasonably long observing times are required for a significant detection of the pulsations of the Crab pulsar with the high-energy-range sub-arrays. We also found that an independent VHE timing analysis is feasible with Large Size Telescopes. CTA will provide a significant improvement in determining the VHE pulse shape parameters necessary to constrain theoretical models of the gamma-ray emission of the Crab pulsar. One of such parameters is the shift in phase between peaks in the pulse profile at VHE and in other energy bands that, if detected, may point to different locations of the emission regions.

Key words: pulsars: individual: Crab pulsar – gamma-rays: stars.

1 INTRODUCTION

The Crab pulsar (PSR J0534+2200) was the first pulsar to be detected by Cherenkov telescopes at very high energy (VHE) gamma-rays above a few tens of GeV (e.g. Aliu et al. 2008, 2011; Aleksić et al. 2011, 2012b). It is the compact remnant of a supernova which exploded approximately 1000 yr ago at a distance of about 2 kpc from the Sun. The magnetic field of the pulsar is 3.8×10^{12} G, its rotational period ∼33.62 ms, and its spin-down power $\sim 4.6 \times 10^{38}$ erg s^{-1} (Manchester et al. 2005). The Crab pulsar is detected at all wavelengths from radio to TeV gamma-rays.

Investigating the pulse profile of pulsars in different energy bands is important in order to fully understand the physical mechanisms responsible for accelerating particles to relativistic energies. Several groups have studied the pulse profile of the Crab pulsar at different energies. The timing properties in the radio band were investigated with a number of radio telescopes, including the Nançay French telescope (Theureau et al. 2005) and the Jodrell Bank Observatory (Hobbs et al. 2004). Some of the most accurate optical observations of the Crab pulsar, with time resolutions of hundreds of picoseconds, were recently carried out with the Copernico Telescope in Asiago (Germanà et al. 2012) and the New Technology Telescope in La Silla (Zampieri et al. 2014). Detailed X-ray pulse profiles were obtained with the Rossi X-ray Timing Explorer (RXTE; Rots, Jahoda & Lyne 2004) as well as with *Suzaku* (Terada et al. 2008), *Swift* (Cusumano et al. 2012) and *XMM–Newton* (Kirsch et al. 2006). Hard X-ray (100–200 keV) and soft gamma-ray (0.75–30 MeV) observations were carried out with *INTEGRAL* (Mineo et al. 2006) and COMPTEL (Kuiper et al. 2001), respectively. Gamma-ray (>100 MeV) observations were performed by *AGILE* (Pellizzoni et al. 2009) and *Fermi*-LAT (Abdo et al. 2010). Finally, recent observations with ground-based Cherenkov telescopes, such as MAGIC (Aleksić et al. 2012b, 2014; Ansoldi et al. 2016) and the Very Energetic Radiation Imaging Telescope Array System (VERITAS, Aliu et al. 2011), have obtained pulse profiles of the Crab pulsar in VHE gamma-rays.

The gamma-ray spectrum of the Crab pulsar above 10 GeV is not consistent with the exponential or steeper cut-off inferred from *Fermi*-LAT data in the 100 MeV–100 GeV energy range (Abdo et al. 2010). MAGIC and VERITAS observations show that the amplitude of the main pulse of the Crab pulsar is lower than the amplitude of the interpulse contrary to what is observed at lower energies with *Fermi*-LAT.

Although there is still no comprehensive theory that can describe the overall emission properties of the Crab pulsar, VHE observations constrain significantly the models of pulsar emission (e.g.

★ E-mail: aleksandr.burtovoi@studenti.unipd.it (AB); luca.zampieri@oapd.inaf.it (LZ)

Aharonian, Bogovalov & Khangulyan 2012; Lyutikov, Otte & McCann 2012).

The Cherenkov Telescope Array (CTA), currently in the development stage, is a project which aims at building two arrays, one in each hemisphere, of imaging atmospheric Cherenkov telescopes (Actis et al. 2011). This observatory is designed to improve the capabilities of present Cherenkov imaging telescopes (MAGIC, VERITAS and the High Energy Stereoscopic System or H.E.S.S.) and will allow us to explore VHE gamma-ray phenomena in more detail. CTA (North+South) will comprise ∼140 telescopes of three different types (Large, Medium and Small Size Telescopes[1] with diameters of 23, ∼10–12 and 4 m, respectively). This will allow CTA to cover the full sky over the energy range from a few tens of GeV to more than 100 TeV (Acharya et al. 2013; Bernlöhr et al. 2013) and to reach 10 times better sensitivity and angular resolution compared to present Cherenkov telescopes installations. There is a possibility of dividing the whole array into different sub-arrays corresponding to different mirror sizes: the LST-array, the MST-array and the SST-array consisting of only Large, Medium and Small Size Telescopes, respectively.

As part of the CTA project, a dual-mirror prototype of the SST is under development within the framework of the ASTRI (*Astrofisica con Specchi a Tecnologia Replicante Italiana*) flagship project of the Italian Ministry of Research and Education led by INAF (La Palombara et al. 2014). This project foresees the construction of a mini-array of nine telescopes, the ASTRI mini-array (Vercellone et al. 2015), possibly as a first segment of the southern CTA installation.

The first comprehensive investigation of prospects for VHE observations of pulsars (including the Crab pulsar) is reported in de Oña-Wilhelmi et al. (2013). The unprecedented sensitivity achievable with CTA prompted us to perform a quantitative investigation of the pulse shape and timing of the Crab pulsar at VHE attainable with the CTA observatory. To estimate the impact of CTA, various simulations were performed for different array configurations and exposure times.

The outline of the paper is as follows. In Section 2, we present the algorithm used to simulate Crab pulsar observations with CTA. A short description of the different CTA configurations is given in Section 3. The pulse profiles resulting from the simulations are presented in Section 4. In Section 5 we discuss our results, while conclusions follow in Section 6.

2 VHE PULSE PROFILE OF THE CRAB PULSAR

The Crab pulsar region has been observed with several VHE telescopes (H.E.S.S., Aharonian et al. 2006; Abramowski et al. 2014; HEGRA, Aharonian et al. 2004; Whipple, Weekes et al. 1989; Grube 2008; CAT, Masterson & CAT Collaboration 2001; MAGIC, Aleksic et al. 2012b, 2014, 2015, Ansoldi et al. 2016; VERITAS, Aliu et al. 2011). For the sake of comparison, in the following we will consider as reference the observations carried out with the two MAGIC telescopes located in La Palma during the period between the winter season 2009/2010 and that of 2010/2011 (Aleksić et al. 2012b). The energy range is 50–400 GeV. A light curve was obtained by phase folding approximately 73 h of observations and is shown in Fig. 1. The light curve can be quite reasonably reproduced by the sum of Gaussian functions plus a constant. Three Gaussians are sufficient for an accurate fit: the first two components correspond to the pulsar peaks (P1 and P2), while the third one (with negative amplitude) improves the fit in the off-pulse interval between 0.52 and 0.87. The adopted fitting function written as a function of phase ϕ is

$$I(\phi) = \sum_{i=1}^{3} k_i G_{m_i,s_i}(\phi) + C, \quad (1)$$

where $G_{m_i,s_i}(\phi) = 1/(\sqrt{2\pi}s_i)\exp[-(\phi - m_i)^2/(2s_i^2)]$ is a Gaussian function with mean m_i, standard deviation s_i and normalization k_i (Table 1), while the constant C accounts for the background. Taking m_i, s_i, k_i and C as free parameters, the MAGIC pulse profile is well fitted by equation (1) with a reduced χ^2 of 1.07. Hereafter we fix the values of the parameters obtained from the fit and use them in the simulations of pulse profiles of the Crab pulsar as would be observed with CTA.

To simulate the pulse profile observed by a CTA-like instrument we calculate the background level $I_{\rm BG}^{\rm M}$ of the MAGIC data in the off-pulse region from phase 0.52 to 0.87 and subtract it from the fitted profile I. Then, we rescale the profile I according to the different effective area $A_{\rm eff}$ of the CTA configurations and to the different observation durations $t_{\rm obs}$. We also assume that the pulse shape does not strongly depend on energy between 0.01 and ∼100 TeV, which allows us to rescale the profile with the number of counts in different spectral bands. Although there is some evidence of evolution of the pulse shape in gamma-rays (e.g. Aleksić et al. 2014), this appears to be in the direction of increasing the significance of the interpulse (with respect to the main pulse). Thus, the actual detection of the

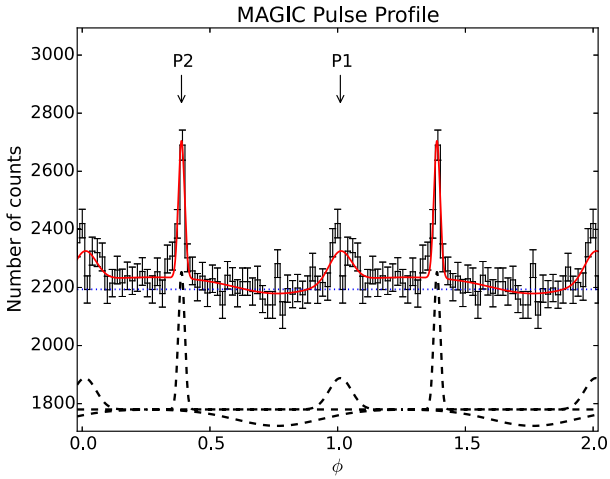

Figure 1. MAGIC 50–400 GeV pulse profile of the Crab pulsar (Aleksić et al. 2012b), along with the fitting function I (red solid line; see text for details). The black dashed lines represent the Gaussian components of I, while the blue dotted line is the background level. P1 and P2 are the main pulse and interpulse, respectively. The adopted number of bins per period is 51.

Table 1. Parameters of the fitting function I, given by the sum of three Gaussians and a constant. The mean, standard deviation and normalization of the Gaussians are reported in the first, second and third column, respectively. The value of C is listed in the fourth row.

i	m_i	s_i	k_i
1	0.389 ± 0.002	0.012 ± 0.002	14 ± 2
2	1.01 ± 0.02	0.04 ± 0.02	12 ± 7
3	0.76 ± 0.09	0.16 ± 0.13	-23 ± 22
$C = (2.24 \pm 0.01) \times 10^3$			

[1] SSTs are expected to be deployed only at the southern site.

interpulse with CTA, on which we will focus below, may in fact be more significant, and our estimates may then be regarded as conservative. To determine the rescaling factor we need an estimate of the energy spectrum in the CTA energy range, which is the major source of uncertainty in the present calculation.

Assuming that $F(E)$ is an appropriate representation of the actual phase-averaged pulsar spectrum in the CTA energy range, we can then rescale the pulse shape according to the following expression:

$$I' = I \times \frac{\int_{E_{\rm min}}^{E_{\rm max}} F(E)\, A_{\rm eff}(E)\, t_{\rm obs}\, {\rm d}E}{\int_{E_{\rm min}^{\rm M}}^{E_{\rm max}^{\rm M}} F_{\rm M}(E)\, A_{\rm eff}^{\rm M}(E)\, t_{\rm obs}^{\rm M}\, {\rm d}E}, \quad (2)$$

where $F(E)$ ($F_{\rm M}(E)$) is the CTA (MAGIC) spectrum, $E_{\rm min}$ ($E_{\rm min}^{\rm M}$) and $E_{\rm max}$ ($E_{\rm max}^{\rm M}$) bracket the corresponding energy range, $A_{\rm eff}$ ($A_{\rm eff}^{\rm M}$) and $t_{\rm obs}$ ($t_{\rm obs}^{\rm M} = 72.78$ h) are the effective area and corresponding observing time in the CTA (MAGIC) configuration. The rescaling factor (the ratio of the two integrals) is determined by comparing the number of counts of the simulated configuration with that of MAGIC. The calculation is done adopting effective areas for similar zenith angles (20° for CTA and VERITAS, averaged below 30° for MAGIC).

For $F(E)$ we assume a power law:

$$F(E) = \frac{{\rm d}N}{{\rm d}E} = N_0 \times \left(\frac{E}{0.1\,{\rm TeV}}\right)^{-\Gamma}, \quad (3)$$

where N_0 and Γ are the normalization and spectral index, respectively. The values of N_0 and Γ are taken from Aleksić et al. (2012b): $N_0 = (13.0 \pm 1.6) \times 10^{-11}$ TeV^{-1} cm^{-2} s^{-1} and $\Gamma = 3.57 \pm 0.27$.[2] We do not use values from the recent work by Ansoldi et al. (2016) because we need spectral parameters averaged over the emission of the two peaks, while they analysed the main pulse and interpulse separately.

Another parameter required to estimate the actual light curve observed with CTA is the background emission, which is generally dominated by the Crab nebula rather than by backgrounds particles (hadrons, electrons and diffuse gamma-rays). We determine it by adopting a simplified approach, similar to that outlined above for rescaling the source counts since, at CTA resolution, both the pulsar and surrounding nebula can be considered as point-sources. Assuming that the VHE emission of the Crab nebula dominates over cosmic ray background up to the ∼100 TeV, the background is obtained by re-normalizing the counts of the Nebula spectrum in the different energy ranges (similar to equation 2):

$$I_{\rm BG} = I_{\rm BG}^{\rm M} \times \frac{\int_{E_{\rm min}}^{E_{\rm max}} F_{\rm BG}(E)\, A_{\rm eff}(E)\, t_{\rm obs}\, {\rm d}E}{\int_{E_{\rm min}^{\rm M}}^{E_{\rm max}^{\rm M}} F_{\rm BG}(E)\, A_{\rm eff}^{\rm M}(E)\, t_{\rm obs}^{\rm M}\, {\rm d}E}, \quad (4)$$

where $I_{\rm BG}^{\rm M}$ is the MAGIC background, measured in the off-pulse region from phase 0.52 to 0.87 (blue dotted line in Fig. 1; Aleksić et al. 2012b). For the nebular spectrum $F_{\rm BG}(E)$, we take the log-parabola approximation of Aleksić et al. (2015):

$$F_{\rm BG}(E) = (3.23 \pm 0.03) \times 10^{-11} \times \left(\frac{E}{1\,{\rm TeV}}\right)^{-(2.47\pm0.01)-(0.24\pm0.01)\log(E/1\,{\rm TeV})} {\rm TeV}^{-1}{\rm cm}^{-2}{\rm s}^{-1}. \quad (5)$$

Summarizing, we generate the simulated pulse profile I_s detected by CTA using the following procedure.

(i) We approximate the pulse profile of the Crab pulsar with the fitting function I (equation 1 and Fig. 1).

[2] Only statistical errors are quoted.

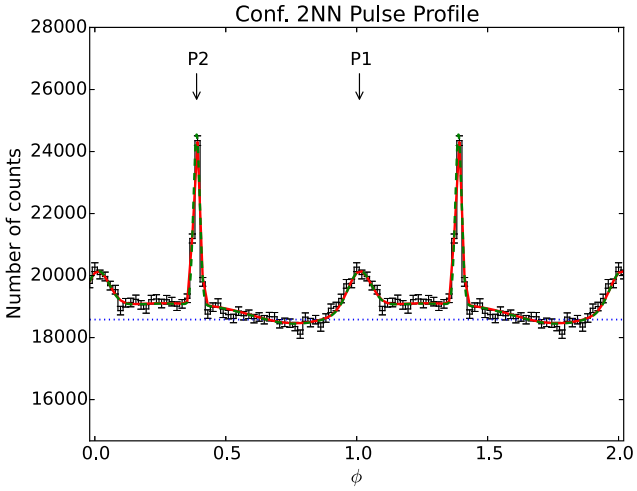

Figure 2. Simulated (I_s, black histogram) and assumed CTA pulse profile (I', red line) of the Crab pulsar detected by Conf. 2NN during an observation with duration $t_{\rm obs}^{\rm M} = 72.78$ h and using 51 bins per period. The green dashed line is a best fit with three Gaussians of the simulated pulse profile. The blue dotted line is the background level. P1 and P2 represent the main pulse and interpulse, respectively.

(ii) We then calculate the MAGIC background level $I_{\rm BG}^{\rm M}$ in the off-pulse region from phase 0.52 to 0.87 and subtract it from the pulse profile I. With this value we then computed the rescaled pulse shape I' from equation (2).

(iii) We calculate the CTA background level $I_{\rm BG}$ from equation (4) and add it to the pulse profile I'.

(iv) Stochastic properties are added to the pulse shape I' to produce the final simulated signal I_s. The simulated pulse profile in the ith bin, $I_{s,i}$, is considered to be a random value following a Gaussian distribution with mean value equal to I' and standard deviation equal to $\sqrt{I'}$. The error in each bin is the square root of the number of counts in that bin, $\sqrt{I_{s,i}}$. An example of the final simulated pulse profile is shown in Fig. 2.

3 CTA AND ASTRI MINI-ARRAY CONFIGURATIONS

Simulated pulse profiles of the Crab pulsar were computed for different sub-arrays of CTA. The corresponding configurations and their properties are listed in Table 2. We consider standard arrays and sub-arrays, which consist of telescopes of different sizes (LSTs and MSTs) distributed according to Monte Carlo (MC) PROD2 configuration (Conf.) 2NN, representative of the northern CTA installation (from LEONCITO++ MC PROD2 DESY package[3]). We also consider sub-arrays with identical types of telescopes, such as Large Size Telescopes (2NN-LST or LST-array) and Medium Size Telescopes (2NN-MST or MST-array). In addition, Conf. 2e – a possible configuration of CTA-South – is of great interest and is then included for comparison.[4] Finally, we use a distribution of nine identical 4 m SSTs with a separation of 257 m (Conf. s9-4-257m) as an

[3] Package (2014 September) available at http://www.cta-observatory.org/ctawpcwiki/index.php/WP_MC#Interface_to_WP_PHYS.

[4] We note that calculations for this configuration are performed for a fixed zenith angle (20°). Although for CTA-South this is smaller than the actual zenith angle of the Crab pulsar, such simulations are performed only for comparison purposes and are not meant to provide detailed quantitative assessments of the pulse profile, detected at the southern installation.

Table 2. Configurations of MAGIC, VERITAS and different sub-arrays of CTA simulated in MC PROD2.

Name	Telescopes	Energy range (TeV)	$E_{\rm thr}$ (TeV)	$\langle A_{\rm eff}\rangle_{\rm sp}$ ($10^5 \times$ m^2)
MAGIC	2 × 17 m	0.05–0.4	0.072	0.07
VERITAS	4 × 12 m	0.1–0.4	0.136	0.28
LST-array	4 LST	0.04–158	0.040	0.49
MST-array	14 MST	0.1–158	0.158	0.71
Mini-array	9 SST	1.6–158	3.981	0.71
Conf. 2NN	4 LST 14 MST	0.04–158	0.040	0.53
Conf. 2e	4 LST 24 MST 72 SST	0.04–158	0.040	0.50

Notes. Configurations 2NN, LST-array and MST-array refer to the northern CTA installation. Conf. 2e corresponds to CTA-South. These configurations are taken from the MC PROD2 DESY simulation package (http://www.cta-observatory.org/ctawpcwiki/index.php/WP_MC#Interface_to_WP_PHYS). LST: Large Size Telescope with diameter 23 m. MST: Medium Size Telescope with diameter 12 m. SST: Small Size Telescope with diameter 4 m. As the best representation for the ASTRI mini-array (Mini-array), we consider a configuration of nine SSTs from the same MC PROD2 simulations (Conf. s9-4-257m). The energy ranges for all these configurations are taken from the corresponding IRFs, while those of MAGIC and VERITAS correspond to the energies at which the Crab pulsar spectrum was measured (see Aleksić et al. 2012b and Aliu et al. 2011, respectively). $E_{\rm thr}$ is the energy threshold, while $\langle A_{\rm eff}\rangle_{\rm sp}$ is the spectrum-weighted effective area of each configuration.

appropriate representation of the ASTRI mini-array in the present MC PROD2 package.

The effective areas $A_{\rm eff}(E)$ and energy ranges ($E_{\rm min}$, $E_{\rm max}$) needed for the convolution with the source and background spectra (equations 2 and 4) are inferred from the instrument response functions (IRFs) and are reported in Table 2. They are calculated from simulations of 50 h observations of a source emitting 1 Crab Unit[5] at a 20 deg zenith angle and with a sensitivity averaged over north and south pointings. For the effective areas of MAGIC ($A^{\rm M}_{\rm eff}(E)$) and VERITAS ($A^{\rm V}_{\rm eff}(E)$), we adopt published values from Aleksić et al. (2012a) and Kieda D. B. for the VERITAS Collaboration (2013), while for the corresponding energy ranges, in which the Crab pulsar spectra were measured, we refer to Aleksić et al. (2012b) and Aliu et al. (2011).

In Table 2, we report also the threshold energy $E_{\rm thr}$ and the spectrum-weighted effective area $\langle A_{\rm eff}\rangle_{\rm sp}$ of each configuration. The former is the energy at which the product of the effective area with the source spectrum $F(E)$ (defined in Section 2) peaks, while the latter is defined as

$$\langle A_{\rm eff}\rangle_{\rm sp} = \frac{\int_{E_{\rm min}}^{E_{\rm max}} A_{\rm eff}(E)F(E){\rm d}E}{\int_{E_{\rm min}}^{E_{\rm max}} F(E){\rm d}E}\,. \quad (6)$$

The values of $E_{\rm thr}$ for MAGIC and VERITAS are consistent with the corresponding values reported in Aleksić et al. (2012a) and Aliu et al. (2011), respectively.

4 RESULTS

Simulated pulse profiles for each CTA array configuration are computed as described in Section 2 and are then fitted with the model function in equation (1). An example of such a calculation is shown in Fig. 2 for CTA Conf. 2NN.

[5] 1 Crab Unit $= 2.79 \times 10^{-11} \times (E/1{\rm TeV})^{-2.57}$ cm^{-2} s^{-1} TeV^{-1}.

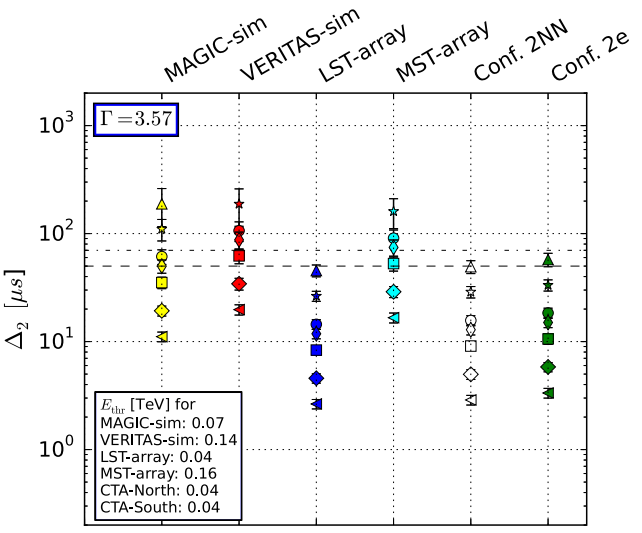

Figure 3. Uncertainty in the position of the interpulse P2 (Δ_2) of the VHE profile of the Crab pulsar, simulated for MC PROD2 Conf. 2NN (white) and for Conf. 2e (green). Results for MAGIC (yellow), VERITAS (red) and the CTA LST-array (blue) and MST-array are also shown. The spectral index of the Crab pulsar spectrum used in these simulations is $\Gamma = 3.57$ (see Section 2). Different markers correspond to observations of different durations in units of the MAGIC observing time ($t^{\rm M}_{\rm obs} = 72.78$ h): 0.1 (triangles), 0.3 (stars), 1 (circles), 1.5 (thin diamonds), 3 (squares), 10 (diamonds), 30 (rotated triangles). Error bars represent the standard deviation calculated from a set of simulations. The dashed and dot–dashed lines show the uncertainties of the MAGIC ($\Delta_2 = 50$ μs; Aleksić et al. 2012b) and VERITAS ($\Delta_2 = 70$ μs; Aliu et al. 2011) observations, respectively.

An important quantity to constrain the parameters (e.g. the height and location of the emission region) of pulsar models is the difference in the time of arrival of the peaks in different energy bands (e.g. Oosterbroek et al. 2008; Aharonian et al. 2012). At optical wavelengths Shearer et al. (2003) and Hinton et al. (2006) found a radio delay between the time of arrival of the optical and radio peaks of the order of 100 μs with an uncertainty of a few tens of microseconds, whereas no delay (-60 ± 50 μs) was found by Golden et al. (2000). While a secular change of this delay may be possible, within measurement uncertainties present observations appear to give delays consistently of the order of ∼150–250 μs, with the optical leading the radio (e.g. Oosterbroek et al. 2008; Zampieri et al. 2014).

Measuring an accurate time differences at VHE requires not only a precise time stamp (in CTA it will be of the order of ns), but also a good signal-to-noise ratio, or in other words good sensitivity. To check how well CTA can measure the peak positions with different observing times, we determined the position of the interpulse P2 and its error (Δ_2) for the CTA sub-arrays considered here. Results are shown in Fig. 3. The value of the uncertainty Δ_2 clearly affects the accuracy with which it will be possible to perform this type of measurement.

For each configuration we repeated the simulations several times and then computed the average Δ_2 and its statistical uncertainty. As can be seen from Fig. 3, the accuracy of the pulse shape attainable by the CTA-North Conf. 2NN is such that even rather short observations (several hours; triangles) are sufficient to measure the position of the interpulse rather accurately. As a consistency

check, we also simulated the MAGIC and VERITAS pulse profile. The simulated 73 h MAGIC observations give results comparable to those of the real 73 h observation ($\Delta_2 = 60 \pm 9$ µs versus ∼50 µs). Similar conclusions are reached for the simulations of the 110 h VERITAS observations ($\Delta_2 = 90 \pm 20$ µs versus ∼70 µs).

We found that observations of short duration with VERITAS ($0.1 \times t_{\rm obs}^{\rm M}$), the MST-array ($0.1 \times t_{\rm obs}^{\rm M}$) are not sufficient to detect significant pulsations. Indeed, in these cases the energy threshold is higher than that of MAGIC. Simulations performed for the high-energy-range arrays containing only SSTs (e.g. ASTRI mini-array) with $E_{\rm thr} > 1$ TeV yield no detection of pulsations even for very long observing times ($30 \times t_{\rm obs}^{\rm M}$) and, therefore, are not shown in Fig. 3. For the ASTRI mini-array significant pulsations are detected only for unrealistically long observing times of more than $\sim 10^6$ h.

In addition to the array configurations listed above, we repeated the simulations for different energy ranges of Conf. 2NN and also for other CTA configurations, such as Confs. 2Nc, 2Ne, 2Nb, 2Nd, 2Nf – representatives of the northern CTA installation – and Confs. 2b, 2c – possible layouts of CTA-South. Results are reported in Appendix A.

We investigated the possibility of measuring an energy dependent shift in the position of the interpulse with different CTA sub-arrays. In particular, we study whether it would be possible to measure phase shifts in the pulse profile among arrays made entirely by different types of telescopes (LSTs, MSTs, SSTs), which are most sensitive in the different energy ranges. This measurement is feasible in ∼73 h with the LSTs and MSTs, but not with the SSTs (because of the larger amount of time required for such array to detect pulsations, see Section 5 for details). The uncertainty in measuring the position of the peak of the pulse profile with the LST- and MST- arrays is $\Delta_2 \sim 14$ µs and $\Delta_2 \sim 90$ µs, respectively (blue and cyan circles in Fig. 3). Therefore, the error on the measurement of the shift between the time of arrival of the LST and MST interpulses is about $\sqrt{14^2 + 90^2} \approx 90$ µs. Any potential phase shift larger than 3×90 µs (=270 µs) between the pulses measured at ∼40 GeV with the LSTs and at ∼100 GeV with the MSTs would be measurable in 73 h at the 3σ confidence level.

We also performed similar simulations using different values of the spectral index Γ (3.0, 3.2, 3.5, 3.8) of the Crab pulsar. For each Γ we calculate the normalization factor N_0, stating that the flux in the energy range from 0.05 to 0.4 TeV is equal to that obtained with MAGIC in the same energy interval (Aleksić et al. 2012b). The values of Δ_2 resulting from the simulations of 73 h observations for all configurations from Table 2 in their full energy range and for simulations restricted to the low (0.04–0.1 TeV)- and mid (0.1–1 TeV)-energy ranges are shown in Figs 4, 5 and 6, respectively. The results of 730 h observations at energies from 1 to 10 TeV are reported in Fig. 7.

4.1 VHE timing analysis

The quality of the pulse shape obtained with the LST-array suggests that a VHE timing analysis of the Crab pulsar, similar to that performed at lower energies (radio/optical/X-ray/low-energy gamma-ray bands), is possible with CTA. We attempted to perform such an analysis of the simulated pulse profile using an approach similar to that discussed in Germanà et al. (2012) and Zampieri et al. (2014).

The time required for the LST-array to achieve statistically significant detection of the pulsar period and the pulse shape is ∼1 h. From the period derivative of the Crab pulsar, one can estimate the phase drift during time Δt as $\Delta\phi_{\rm drift} \approx \dot{\nu}\Delta t^2/2$. Assuming $\dot{\nu} \approx -3.7 \times 10^{-10}$ s^{-2} (see e.g. Zampieri et al. 2014) and

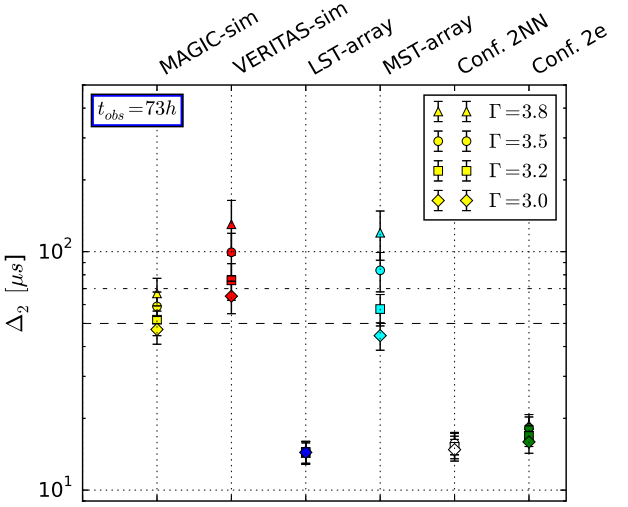

Figure 4. Uncertainty in the position of the interpulse P2 (Δ_2) of the VHE profile of the Crab pulsar for different values of the spectral index Γ: 3.8 (triangles), 3.5 (circles), 3.2 (squares), 3.0 (diamonds). Results for MAGIC (yellow), VERITAS (red), the LST-array (blue), the MST-array (cyan), Conf. 2NN (white) and Conf. 2e (green) are shown. Simulations are performed in the full energy range of each configuration. Observing time is $t_{\rm obs}$ = 73 h. Error bars represent the standard deviation calculated from a set of simulations. The dashed and dot–dashed lines show the uncertainties of the MAGIC ($\Delta_2 = 50$ µs; Aleksić et al. 2012b) and VERITAS ($\Delta_2 = 70$ µs; Aliu et al. 2011) observations, respectively.

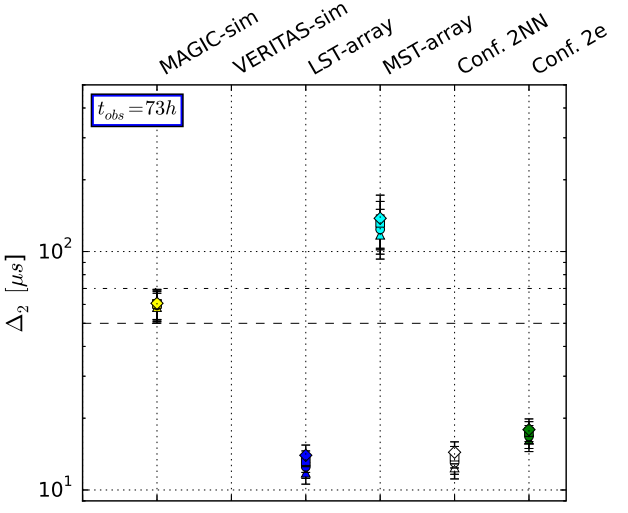

Figure 5. Same as Fig. 4, but restricted to the low-energy range (0.04–0.1 TeV).

$\Delta t = 3$ h, we find $|\Delta\phi_{\rm drift}| \approx 0.02$, value comparable to the bin size adopted here ($1/N_{\rm bins}$). Therefore, no more than three consecutive 1 h observations can be performed without a significant phase drift of the Crab pulsar pulse profile.

We investigated the phase drift of the interpulse P2 (more prominent at VHE than the main pulse), measured with short LSTs observations during a number of consecutive nights. Such measurements require an accurate initial estimate of the Crab pulsar period. For each night, we simulate three 1 h observations assuming a parabolic law for the phase drift:

$$\psi(t) = \phi_0 + a(t - t_0) + b(t - t_0)^2 , \quad (7)$$

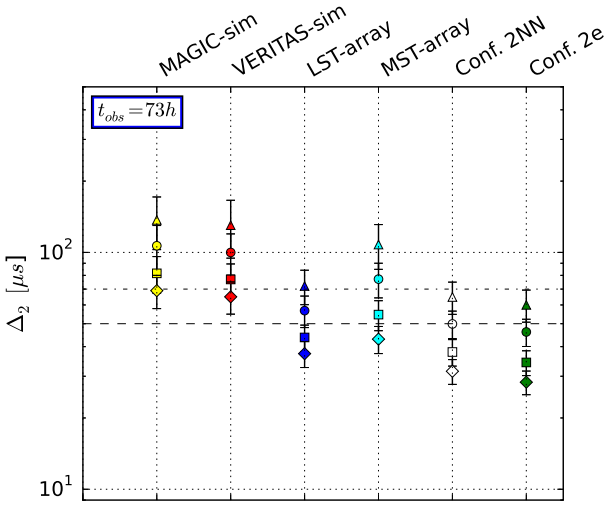

Figure 6. Same as Fig. 4, but restricted to the mid-energy range (0.1–1 TeV).

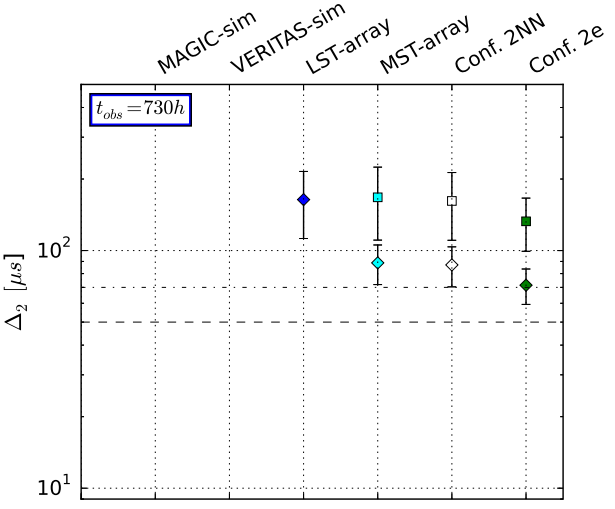

Figure 7. Same as Fig. 4, but restricted to the high-energy range (1–10 TeV) and for the observing times of $t_{\rm obs} = 730$ h.

where ϕ_0 is the pulsar phase at t_0, $a = (\nu_0 - \nu_{\rm init})$ is the difference between the rotational frequency of the pulsar ν_0 at t_0 and a reference frequency $\nu_{\rm init}$. b is equal to $\dot{\nu}_0/2$, where ν_0 is the rotational frequency first derivative at t_0. $\nu_{\rm init}$ is the reference frequency used to fold the data. In our analysis, we assume that the difference between ν_0 and $\nu_{\rm init}$ is of the order of 10^{-5} s^{-1} and that $\dot{\nu}_0 \simeq -3.7 \times 10^{-10}$ s^{-2} (see e.g. Germanà et al. 2012 or Zampieri et al. 2014). The adopted values of ϕ_0, a and b are reported in the first line of Table 3. In order to accurately fold real data, it will require changing reference frequency each night. It is possible to reduce the phase measurements to a single reference frequency using the method described in Zampieri et al. (2014).

Following the procedure described in Section 2, for each observation we simulated the pulse profile detected with the LST-array[6] and obtained the phase drift ψ_i and error σ_i of the interpulse in the ith observation. Typically, $\sigma_i \sim 120$ μs. We then simulated two and three nights of observations of the Crab pulsar (see Figs 8 and 9). The positions of the interpulse, derived from the simulated observations and reduced to the same reference frequency, were then fitted with the parabolic law in equation (7). Best-fitting coefficients and corresponding errors are reported in Table 3 (second and third lines). From these values it is possible to estimate the accuracy in determining the time of arrival of the interpulse, which is ∼140 μs after two nights and ∼80 μs after three nights

[6] For these simulations we assume a power-law spectrum for the Crab pulsar with $N_0 = 13.0 \times 10^{-11}$ TeV^{-1} cm^{-2} s^{-1} and $\Gamma = 3.57$.

Table 3. Parameters of the parabolic fit of the phase drift. The first line shows the assumed spin-down law, while the second and third lines contain the best-fitting values of the parameters obtained from a fit of the simulated spin-down for two different observing intervals (two nights and three nights; see text for details).

	ϕ_0	a (10^{-5} s^{-1})	b (10^{-10} s^{-2})
ψ	0.394	1.0	−1.85
$\psi_{\rm 2d}$	0.386±0.004	1.05 ± 0.06	−1.90±0.06
$\psi_{\rm 3d}$	0.390±0.002	0.995 ± 0.006	−1.847±0.003

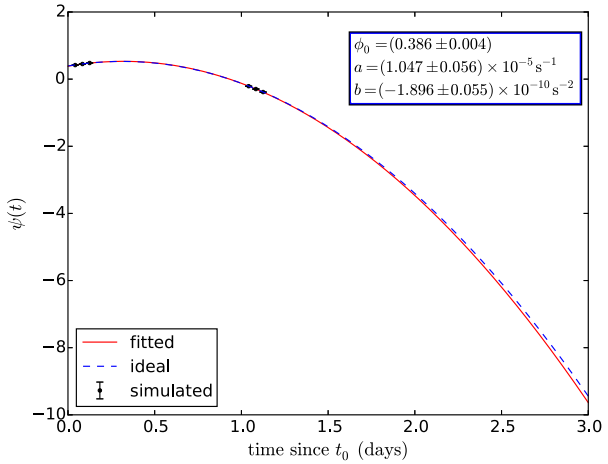

Figure 8. Simulated phase drift of the VHE interpulse of the Crab pulsar observed with the LST-array over two nights. The blue dashed line is the assumed spin-down law. The red solid line is the best-fitting parabola. Black dots are the simulated data.

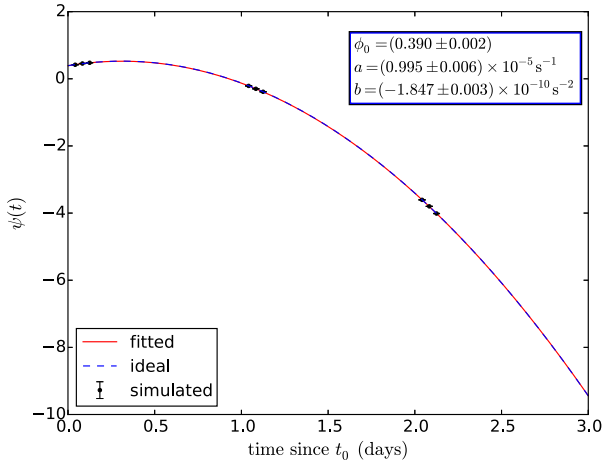

Figure 9. Same as Fig. 8 for observations covering three nights.

(assuming $P(t_0) = 0.03362$ s, which is the approximate rotational period of the Crab pulsar at t_0, see e.g. Zampieri et al. 2014). Increasing the number of observing nights does not improve significantly the accuracy of the fitting parameters (e.g. the accuracy in determining the position of the interpulse is ∼65 μs after seven nights).

For the MSTs and SSTs this type of measurements of the phase drift of the interpulse is not feasible because detecting a pulse profile requires more than one observing night.

5 DISCUSSION

We performed simulations of the VHE gamma-ray pulse profile of the Crab pulsar for different configurations of CTA and the ASTRI mini-array, therefore in intrinsically different energy ranges and with different observing times. The LSTs, MSTs and SSTs will probe different spectral regions (from a few tens of GeV up to several tens of TeV) with different sensitivities (Bernlöhr et al. 2013). For all simulated pulse profiles we determined the uncertainty Δ_2 in the position of the interpulse.

As shown in Fig. 3, the LST-array reaches the same accuracy as MAGIC ($\Delta_2 \sim 50$ μs) but in a much shorter observation time ($0.1 \times t^{\rm M}_{\rm obs}$). 73 h of observations with the same configuration lead to an uncertainty in the peak position of 14 μs. Observations with the northern configuration Conf. 2NN give an improvement by a factor ∼3 in accuracy as compared to MAGIC (with 73 h of observing time; see again Fig. 3). Similar values of Δ_2 are obtained for the full-energy-range configurations Conf. 2e, which contains all three types of telescopes. These results are slightly worse than that attainable with the LST-array because of the lower background contamination and larger effective area of the latter configuration in the energy range below a few hundred GeV, where the Crab pulsar is easier to detect due to its steep spectrum.

The quality of the measured pulse shape decreases significantly above 1 TeV again because of the steeply falling spectrum. In spite of the increase in the effective area with energy, the value of Δ_2 for the MST-array measured above 100 GeV is nearly the same as that of MAGIC above 50 GeV. This is even more the case for the high-energy-range array of SSTs. We estimated, that only with a 10^4 times longer observing time ($\sim 7 \times 10^5$ h), will an array of 72 SSTs return a value of Δ_2 (above a few TeV) comparable with that of VERITAS above 100 GeV. Similar conclusions can be drawn for the ASTRI mini-array, which contains only nine SSTs. Pure detection of the pulsed emission in this case would require $\sim 10^6$ h and is thus not achievable.

We note that all estimates depend on the values of the effective area and energy threshold. Modifications of the telescopes design and arrays configurations can affect them and, therefore, change the results presented here.

Clearly, these results are very sensitive also to the VHE spectral index Γ of the Crab pulsar. We performed similar simulations assuming different values of Γ (3.0, 3.2, 3.5, 3.8) in the full (0.04–160 TeV), low (0.04–0.1 TeV)-, mid (0.1–1 TeV)- and high (1–10 TeV)-energy ranges (see Figs 4–7). Below 100 GeV the best Δ_2 is provided by the LST-array. In the energy range 0.1–1 TeV the most accurate values of Δ_2 are obtained with Conf. 2NN – the northern CTA installation, which contains LSTs and MSTs – and with Conf. 2e, which comprises all three types of telescopes (LSTs, MSTs, SSTs). Even if the spectrum of the Crab pulsar is rather steep ($\Gamma = 3.8$) in this energy range, CTA will be able to reach an accuracy $\Delta_2 \sim 60$ μs in 73 h (see green triangle in Fig. 6). However, above 1 TeV only with 10 times longer observations (730 h) and assuming a hard spectrum for the Crab pulsar ($\Gamma = 3.0$), will Conf. 2e perform an accurate measurement of the position of the interpulse P2 ($\Delta_2 = 70$ μs).

Theoretical models predict different spectral behaviours of isolated pulsars at VHE. Aharonian et al. (2012) presented a mechanism of VHE gamma-ray production through inverse Compton (IC) scattering of X-ray photons on relativistic electrons, accelerated in a region located far beyond the light cylinder of the neutron star (from $20R_L$ to $50R_L$, where R_L is a light-cylinder radius). This model predicts a cut-off at 500 GeV. Lyutikov et al. (2012) showed that ultraviolet and X-ray photons produced in the inner magnetosphere can be up-scattered to VHE in the outer magnetosphere and produce a spectral tail extending up to ∼15 TeV (if the accelerating electric field is 100 times lower than the magnetic field of the neutron star, and the curvature radius of the order of the light-cylinder radius R_L). IC scattering on a relativistic electron–positron pair plasma accelerated in annular or core gap regions predicts a VHE gamma-ray spectrum reaching 400 GeV (Du, Qiao & Wang 2012).

In order to determine the VHE folded profiles needed for the present analysis, an accurate knowledge of the Crab pulsar ephemerids is required. This can be obtained from simultaneous observations at lower energies (e.g. radio, optical). However, we also investigated the possibility of performing an independent phase timing analysis at VHE only with CTA, using observations spread over several nights. The strategy is similar to that adopted in Germanà et al. (2012) and Zampieri et al. (2014). We simulated two- and three-night observations with the LST-array (three 1 h exposures each night). The accuracy on the time of arrival of the interpulse is ∼140 μs and ∼80 μs for observations covering two or three nights, respectively. Resulting values are worse than those derived from a fit of the pulse profile obtained folding together all observations (using known ephemerides). Thus, although an independent VHE timing analysis based on short repeated observations appears to be feasible with the LSTs, for the sake of measuring Δ_2 the obtained results are less accurate.

6 CONCLUSIONS

The energy spectrum and pulse profile at VHE are crucial ingredients for any comprehensive theory of pulsar emission. Different mechanisms for particle acceleration and VHE gamma-ray emission have been proposed (see Aharonian et al. 2012; Lyutikov et al. 2012; Mochol & Petri 2015). Some models (see Bai & Spitkovsky 2010) can predict the shape of the pulse profile and yield different time shifts between the position of the peaks at VHE and in the radio band. Because of its better sensitivity and wider energy range CTA will provide crucial input for the theory. Together with the full CTA, the LSTs- and MSTs-arrays will provide an accurate measurement of the time of arrival of the peaks at VHE, and will then allow us to determine its shift with respect to simultaneous measurements in other energy bands (radio, optical, X-rays, low-energy gamma-rays; Abdo et al. 2010). In this respect, it would be important that presently on-going monitoring programmes of the Crab pulsar at different wavelengths (e.g. that of Jodrell Bank in the radio) continue to operate.

Configurations containing LSTs/MSTs (with threshold energy $E_{\rm thr}$ equal to 0.04/0.16 TeV) will be able to measure more detailed features in the VHE pulse profile, which will further constrain the emission region and emission mechanism of pulsars. Any potential phase shift between the LST- and MST-arrays significantly larger than ∼270 μs will also be detectable. On the other hand, extrapolating the power-law spectral shape inferred at lower energies, an

accurate determination of the pulse profile of the Crab pulsar with the high-energy SSTs ($E_{\rm thr} = 1$ TeV) is essentially not possible.

ACKNOWLEDGEMENTS

This work was partially supported by the ASTRI 'Flagship Project' financed by the Italian Ministry of Education, University and Research (MIUR) and led by the Italian National Institute of Astrophysics (INAF). We acknowledge partial support by the MIUR Bando PRIN 2009 and TeChe.it 2014 Special Grants. We also acknowledge support from the Brazilian Funding Agency FAPESP (Grant 2013/10559-5) and from the South African Department of Science and Technology through Funding Agreement 0227/2014 for the South African Gamma-Ray Astronomy Programme. We gratefully acknowledge support from the agencies and organizations listed under Funding Agencies at http://www.cta-observatory.org/ and from the University of Padova.

REFERENCES

Abdo A. A. et al., 2010, ApJ, 708, 1254
Abramowski A. et al., 2014, A&A, 562, L4
Acharya B. S. et al., 2013, Astropart. Phys., 43, 3
Actis M. et al., 2011, Exp. Astron., 32, 193
Aharonian F. et al., 2004, ApJ, 614, 897
Aharonian F. et al., 2006, A&A, 457, 899
Aharonian F. A., Bogovalov S. V., Khangulyan D., 2012, Nature, 482, 507
Aleksić J. et al., 2011, ApJ, 742, 43
Aleksić J. et al., 2012a, Astropart. Phys., 35, 435
Aleksić J. et al., 2012b, A&A, 540, A69
Aleksić J. et al., 2014, A&A, 565, L12
Aleksić J. et al., 2015, J. High Energy Astrophys., 5, 30
Aliu E. et al., 2008, Science, 322, 1221
Aliu E. et al., 2011, Science, 334, 69
Ansoldi S. et al., 2016, A&A, 585, A133
Bai X.-N., Spitkovsky A., 2010, ApJ, 715, 1282
Bernlöhr K. et al., 2013, Astropart. Phys., 43, 171
Cusumano G. et al., 2012, A&A, 548, A28
de Oña-Wilhelmi E. et al., 2013, Astropart. Phys., 43, 287
Du Y. J., Qiao G. J., Wang W., 2012, ApJ, 748, 84
Germanà C. et al., 2012, A&A, 548, A47
Golden A., Shearer A., Redfern R. M., Beskin G. M., Neizvestny S. I., Neustroev V. V., Plokhotnichenko V. L., Cullum M., 2000, A&A, 363, 617
Grube J., 2008, Int. Cosm. Ray Conf., 2, 691
Hinton J., Hermann G., Krötz P., Funk S., 2006, Astropart. Phys., 26, 22
Hobbs G., Lyne A. G., Kramer M., Martin C. E., Jordan C., 2004, MNRAS, 353, 1311
Kieda D. B. for the VERITAS Collaboration, 2013, in Proc. 33rd Int. Cosmic Ray Conf., preprint (arXiv:1308.4849)
Kirsch M. G. F. et al., 2006, A&A, 453, 173
Kuiper L., Hermsen W., Cusumano G., Diehl R., Schönfelder V., Strong A., Bennett K., McConnell M. L., 2001, A&A, 378, 918
La Palombara N. et al., 2014, in Giani S. et al., eds, Proc. 14th ICATPP Conf., Astroparticle, Particle, Space Physics and Detectors for Physics Applications. World Scientific, Singapore, p. 754
Lyutikov M., Otte N., McCann A., 2012, ApJ, 754, 33
Manchester R. N., Hobbs G. B., Teoh A., Hobbs M., 2005, AJ, 129, 1993
CAT CollaborationMasterson C., 2001, in Aharonian F. A., Völk H. J., eds, AIP Conf. Proc. Vol. 558, High Energy Gamma-Ray Astronomy. Am. Inst. Phys., New York, p. 753
Mineo T., Ferrigno C., Foschini L., Segreto A., Cusumano G., Malaguti G., Di Cocco G., Labanti C., 2006, A&A, 450, 617
Mochol I., Petri J., 2015, MNRAS, 449, L51
Oosterbroek T. et al., 2008, A&A, 488, 271
Pellizzoni A. et al., 2009, ApJ, 691, 1618
Rots A. H., Jahoda K., Lyne A. G., 2004, ApJ, 605, L129
Shearer A., Stappers B., O'Connor P., Golden A., Strom R., Redfern M., Ryan O., 2003, Science, 301, 493
Terada Y. et al., 2008, PASJ, 60, 25
Theureau G. et al., 2005, A&A, 430, 373
Vercellone S., for the ASTRI Collaboration and the CTA Consortium, 2015, in Proc. 'The Roma International Conference on Astroparticle Physics (RICAP) 2014', preprint (arXiv:1508.00799)
Weekes T. C. et al., 1989, ApJ, 342, 379
Zampieri L. et al., 2014, MNRAS, 439, 2813

APPENDIX A: RESULTS FOR OTHER MC PROD2 CONFIGURATIONS

Here, we summarize the results of our simulations for different energy ranges of Conf. 2NN and also for other CTA configurations,

Table A1. Configurations of MAGIC, VERITAS and different sub-arrays of CTA simulated in MC PROD2.

Name	Telescopes	Energy range (TeV)	$E_{\rm thr}$ (TeV)	$\langle A_{\rm eff}\rangle_{\rm sp}$ ($10^5 \times$ m^2)
MAGIC	2 × 17 m	0.05–0.4	0.072	0.07
VERITAS	4 × 12 m	0.1–0.4	0.136	0.28
LST-array	4 LST	0.04–158	0.040	0.49
MST-array	14 MST	0.1–158	0.158	0.71
Mini-array	9 SST	1.6–158	3.981	0.71
Conf. 2NN	4 LST 14 MST	0.04–158	0.040	0.53
Conf. 2Nb	4 LST 14 MST	0.04–100	0.040	0.53
Conf. 2Nc	4 LST 10 MST 10 SST	0.04–158	0.040	0.53
Conf. 2Nd	3 LST 12 MST	0.03–100	0.040	0.53
Conf. 2Ne	3 LST 12 MST	0.04–100	0.040	0.53
Conf. 2Nf	4 LST 10 MST	0.04–100	0.040	0.53
Conf. 2b	3 LST 18 MST 72 SST	0.04–158	0.040	0.24
Conf. 2c	3 LST 32 MST 38 SST	0.04–158	0.040	0.26
Conf. 2e	4 LST 24 MST 72 SST	0.04–158	0.040	0.50

Notes. Confs. 2NN, 2Nc, 2Ne, 2Nb, 2Nd, 2Nf are representatives of the northern CTA installation. Confs. 2b, 2c and 2e refer to CTA-South. All these arrays are taken from the MC PROD2 DESY simulation package (http://www.cta-observatory.org/ctawpcwiki/index.php/WP_MC#Interface_to_WP_PHYS). LST: Large Size Telescope with diameter 23 m. MST: Medium Size Telescope with diameter 12 m. SST: Small Size Telescope with diameter 4 m. As the best representation for the ASTRI mini-array (Mini-array), we consider a configuration of nine SST from the same MC PROD2 simulations (Conf. s9-4-257m). The energy ranges for all these configurations are taken from the corresponding IRFs, while those of MAGIC and VERITAS correspond to the energies at which the Crab pulsar spectrum was measured (see Aleksić et al. 2012b and Aliu et al. 2011, respectively). $E_{\rm thr}$ is the energy threshold, while $\langle A_{\rm eff}\rangle_{\rm sp}$ is the spectrum-weighted effective area of each configuration.

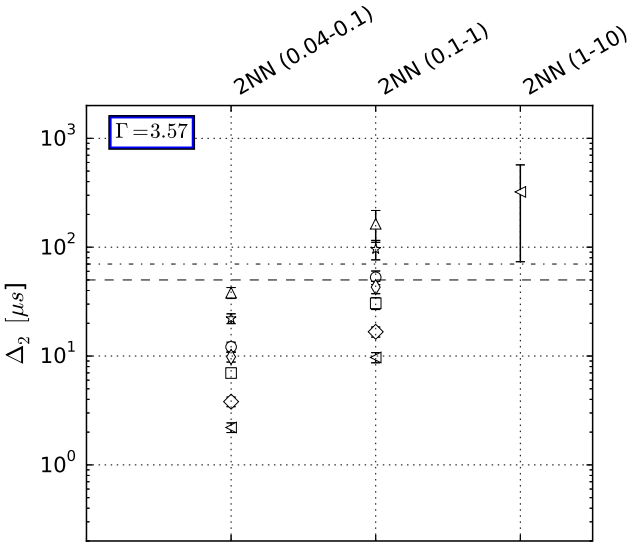

Figure A1. Same as Fig. 3 for different energy ranges of Conf. 2NN.

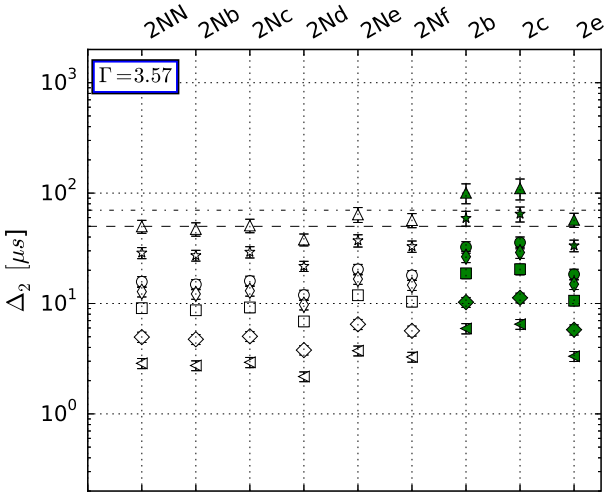

Figure A2. Same as Fig. 3 for other possible layouts of the CTA-North (Confs. 2NN, 2Nc, 2Ne, 2Nb, 2Nd, 2Nf in white) and CTA-South (Confs. 2b, 2c, 2e in green) installations.

such as Confs. 2Nc, 2Ne, 2Nb, 2Nd, 2Nf – representatives of the northern CTA installation – and Confs. 2b, 2c, 2e – possible layouts of CTA-South. The properties of all simulated arrays are listed in Table A1 and the corresponding values of Δ_2 are shown in Figs A1, A2 and Table A2. Observations of short duration with Conf. 2NN ($0.1 \times t^{\rm M}_{\rm obs}$, $0.3 \times t^{\rm M}_{\rm obs}$, $1 \times t^{\rm M}_{\rm obs}$, $1.5 \times t^{\rm M}_{\rm obs}$, $3 \times t^{\rm M}_{\rm obs}$) are not sufficient to detect significant pulsations in the 1–10 TeV energy range.

Table A2. Uncertainty in the position of the interpulse P2 (Δ_2 μs) of the simulated VHE profile of the Crab pulsar, calculated for MAGIC, VERITAS and the different CTA instrumental configurations shown in Figs 3, A1 and A2. Columns refer to different observing times in units of the MAGIC observing time ($t^{\rm M}_{\rm obs} = 73$ h). The spectral index of the Crab pulsar spectrum used in the simulations is $\Gamma = 3.57$ (Aleksić et al. 2012b).

Name	$0.1 \times t^{\rm M}_{\rm obs}$	$0.3 \times t^{\rm M}_{\rm obs}$	$1 \times t^{\rm M}_{\rm obs}$	$1.5 \times t^{\rm M}_{\rm obs}$	$3 \times t^{\rm M}_{\rm obs}$	$10 \times t^{\rm M}_{\rm obs}$	$30 \times t^{\rm M}_{\rm obs}$
MAGIC-sim	190 ± 60	110 ± 25	60 ± 9	50 ± 7	35 ± 4	19 ± 2	11 ± 1
VERITAS-sim	–	190 ± 70	110 ± 20	90 ± 20	62 ± 10	34 ± 4	20 ± 2
LST-array	45 ± 6	26 ± 3	14.5 ± 1.5	12 ± 1	8.3 ± 0.9	4.6 ± 0.5	2.6 ± 0.3
MST-array	–	160 ± 50	90 ± 20	75 ± 12	53 ± 8	59 ± 3	17 ± 2
Conf. 2NN	49 ± 7	30 ± 4	16 ± 2	13 ± 1	9.1 ± 0.9	5.0 ± 0.5	2.9 ± 0.3
– (0.04–0.1 TeV)	38 ± 4	22 ± 2	12 ± 1	9.8 ± 1.0	7.0 ± 0.7	3.8 ± 0.4	2.2 ± 0.2
– (0.1–1 TeV)	160 ± 50	100 ± 20	53 ± 8	43 ± 6	30 ± 4	17 ± 2	10 ± 1
– (1–10 TeV)	–	–	–	–	–	–	320 ± 250
Conf. 2Nb	47 ± 7	27 ± 3	15 ± 2	12 ± 1.2	8.6 ± 0.9	4.7 ± 0.5	2.7 ± 0.3
Conf. 2Nc	51 ± 7	29 ± 3	16 ± 2	13.0 ± 1.4	9.2 ± 1.0	5.0 ± 0.5	2.9 ± 0.3
Conf. 2Nd	38 ± 5	22 ± 2	11.9 ± 1.3	9.8 ± 1.0	6.9 ± 0.7	3.8 ± 0.4	2.2 ± 0.2
Conf. 2Ne	64 ± 10	37 ± 5	20 ± 2	17 ± 2	11.9 ± 1.2	6.5 ± 0.7	3.7 ± 0.4
Conf. 2Nf	57 ± 8	33 ± 4	18 ± 2	14.7 ± 1.7	10.4 ± 1.0	5.7 ± 0.6	3.3 ± 0.3
2b	100 ± 20	59 ± 9	32 ± 4	27 ± 3	19 ± 2	10.3 ± 1.1	5.9 ± 0.6
2c	110 ± 20	65 ± 10	36 ± 4	29 ± 3	20 ± 2	11.3 ± 1.2	6.5 ± 0.7
2e	58 ± 8	33 ± 4	18 ± 2	15.0 ± 1.6	11 ± 1	5.8 ± 0.6	3.3 ± 0.3

Notes. Error bars represent the standard deviation calculated from a set of simulations. The results for the ASTRI mini-array are not shown because the time required for a significant detection is more than $30 \times t^{\rm M}_{\rm obs}$ (see text for details).

This paper has been typeset from a TEX/LATEX file prepared by the author.